Higher-order ferromagnetic resonances in out-of-plane saturated Co/Au magnetic multilayers

L. Fallarino,[1] S. Stienen,[1] R. A. Gallardo,[2,3] J. A. Arregi,[4] V. Uhlíř,[4,5] K. Lenz,[1] R. Hübner,[1] A. Oelschlägel,[1] O. Hellwig,[1,6] and J. Lindner[1]

[1]*Helmholtz-Zentrum Dresden-Rossendorf, Institute of Ion Beam Physics and Materials Research, Bautzner Landstrasse 400, 01328 Dresden, Germany*

[2]*Departamento de Física, Universidad Técnica Federico Santa María, Avenida España 1680, 2390123 Valparaíso, Chile*

[3]*Center for the Development of Nanoscience and Nanotechnology (CEDENNA), 917-0124 Santiago, Chile*

[4]*CEITEC BUT, Brno University of Technology, Purkyňova 123, 612 00 Brno, Czechia*

[5]*Institute of Physical Engineering, Brno University of Technology, Technická 2, 616 69 Brno, Czechia*

[6]*Institute of Physics, Chemnitz University of Technology, D-09107 Chemnitz, Germany*

(Received 25 February 2020; revised 6 August 2020; accepted 1 September 2020; published 25 September 2020)

Artificial ferromagnetic (FM)/nonmagnetic multilayers, with large enough FM thickness to prevent the dominance of interface anisotropies, offer a straightforward insight into the understanding and control of perpendicular standing spin wave (PSSW) modes. Here we present a study of the static and dynamic magnetic properties of $[Co(3.0\,nm)/Au(0.6\,nm)]_{1\leqslant N\leqslant 30}$ multilayers. Magnetometry reveals that the samples exhibit magnetization reversal properties typical of an effective single layer with weak perpendicular anisotropy, with the distinctive thickness-dependent magnetization reorientation transition from uniform in-plane to out-of-plane stripe domains at remanence. However, when such multilayer systems are out-of-plane saturated, the dynamic response reveals the existence of several different ferromagnetic resonances in the form of PSSW modes that strongly depend on the material modulation characteristics along the total thickness. These modes are induced by the layer stacking itself as the effective single layer model fails to describe the observed complex dynamics. In contrast to most systems considered in the past, described by a dynamic model of a single effectively homogeneous thick layer, the specific structures investigated here provide a unique platform for a large degree of tunability of the mode frequencies and amplitude profiles. We argue that the combination of periodic magnetic properties with vertical deformation gradients, arising from heteroepitaxial strain relaxation, converts the Au interlayer regions into a vertical regular array of magnetic pinning planes for the PSSW modes, which promotes the complex dynamics observed in this system.

DOI: 10.1103/PhysRevB.102.094434

I. INTRODUCTION

Multilayer (ML) systems consisting of alternating layers of ferromagnetic (FM) and nonmagnetic (NM) materials have gained steadily growing interest from fundamental physical perspective as well as for technological applications [1–3]. Due to the short- and long-range interactions acting in these MLs, their characteristics can be conveniently modified through small changes in the specifics of the layer stack. Concerning the static magnetic behavior, the uniform out-of-plane (OOP) magnetic ground state may be achieved by appropriately choosing the material parameters, primarily supported by the FM/NM interfaces (surfaces) in the thin film regime [4–7]. An increase of either the thickness of the individual FM layer component or the total number of the FM/NM repetitions, i.e., the total overall thickness, causes the occurrence of nonuniform microscopic magnetization states, resulting in a magnetization reversal process dominated by the collective propagation of OOP domains [8–10]. However, this change could also lead to a complete in-plane (IP) reorientation of magnetization. This may be due to either the absence of a sufficiently high OOP magnetocrystalline anisotropy or an insufficient ML volume, both causing an IP uniform state being preferred over an OOP domain state [11–16]. Indeed, these changes do not only impact the static magnetic properties, but substantially also the dynamic behavior of ML systems.

Out of many experimental methods that have been applied to dynamic studies, ferromagnetic resonance (FMR) has proven to be one of the most powerful tools to sensitively evaluate any change and evolution of magnetic properties [17–22]. While measuring the uniform or quasiuniform resonant mode, information about the volume averaged magnetic properties can be gained. The higher-order modes are instead more sensitive to exchange and anisotropy energies spatially varying across the thickness as well as to OOP magnetic inhomogeneities or modulations within the system [17–23]. Among the latter, perpendicular standing spin wave (PSSW) modes are excitations confined within the thickness of the film. Their wavelengths are usually determined by the total thickness and the magnetization pinning conditions at the top/bottom surfaces, which also govern the energy needed to access and drive the PSSW modes in FM single layers [23–27]. PSSW modes have been already investigated in homogeneous thick films as well as in ML systems to quite some extent [28–34], mainly to study and measure exchange interactions [35,36], exchange stiffness [30,31,37], damping [26,38], and switching field reduction of highly coercive

magnets [39]. However, their behavior in FM/NM systems in the regime of thick individual FM layers—too thick to allow the interface anisotropy to dominate—has not been studied so far. In fact, FM/NM multilayers naturally provide a suitable platform to introduce systematic and regular nonmagnetic interlayerlike pinning planes at their NM interlayer regions throughout the total thickness, otherwise only confined at the top and bottom surfaces of a magnetically homogeneous system. Therefore MLs represent an efficient means to excite and manipulate such exchange-dominated spin-wave modes, which could potentially have implications for novel high-frequency spintronic applications [40,41].

The studied system consists of $[\mathrm{Co}(3.0\,\mathrm{nm})/\mathrm{Au}(0.6\,\mathrm{nm})]_N$ MLs with a variable number of Co/Au bilayers N. We have chosen the individual and total thicknesses such that the interface-induced anisotropy is not primarily driving the static magnetic response. Moreover, we have grown our ML structures on top of a thick Au(111) buffer layer, such that Co, which adopts at room temperature the hexagonal close-packed (hcp) crystal structure and exhibits a magnetic easy axis along the hcp crystal c-axis, grows with the necessary crystallographic texture to induce an OOP anisotropy-axis orientation [11,14–16,42]. We note that similar multilayer sample structures, where the Au(0.6 nm) layers were substituted by Pt(0.6 nm) layers, were already fully statically characterized [42] and provided valuable knowledge for the dynamic studies presented here. Finally, the proposed FMR model is based on the Landau-Lifshitz equation of motion [43] in order to explain the experimental data, where variations of the anisotropy fields along the thickness of the ML structure are included.

The paper is organized as follows. We describe the experimental details in Sec. II. Then, Sec. III A details the identification of the crystal structure and the evaluation of the epitaxial relationships. In Sec. III B, the room-temperature magnetometry characterization is presented, whereas the FMR spectroscopy studies together with analytical calculations are discussed in Sec. III C. Finally, Sec. IV provides a summary of the results and general conclusions.

II. EXPERIMENTAL DETAILS

The samples were grown at room temperature by dc magnetron sputtering in an ultrahigh vacuum system (ATC 2200 series from AJA International, Inc.) with a base pressure better than 3×10^{-6} Pa. Si(001) substrates covered by a 100-nm-thick thermal SiO_x layer were used. Each layer was deposited using a pure Ar pressure of 4×10^{-1} Pa. The $[\mathrm{Co}(3.0\,\mathrm{nm})/\mathrm{Au}(0.6\,\mathrm{nm})]_N$ MLs were grown on Ta(1.5 nm)/Au(20 nm) seed layers. The Au (20 nm) buffer layer serves to maximize the hcp (0001) texture within the Co/Au MLs similar as also done with Pt seed layers in Co/Pt multilayers [42]. The thickness of the Au cap layer was 2.4 nm, which is sufficient to prevent oxidation as well as aging effects after removal from the vacuum system. Au as capping material has also been chosen to avoid breaking the spatial inversion symmetry along the OOP direction of the ML [44–46]. In studies of interlayer exchange coupling, layered systems with Au as a spacer are shown to exhibit Ruderman–Kittel–Kasuya–Yosida (RKKY)-type coupling, and the Au thickness of 0.6 nm, as chosen in this current study, corresponds to ferromagnetic-type interlayer exchange coupling [47–50]. The investigated periods of the ML were $N = 1, 2, 3, 4, 6, 8, 10, 14, 18, 22, 26,$ and 30. A schematic representation of the sample structure, including its specific layer sequence and thicknesses, is shown in Fig. 1. The structural analysis of the samples was performed by means of x-ray diffraction (XRD) and reflectivity (XRR) utilizing a Rigaku SmartLab x-ray thin film diffractometer operated with Cu-K_α radiation. Magnetization measurements were performed using a Microsense EZ7 vibrating sample magnetometer (VSM), equipped with a 360° rotational stage. The dynamic magnetic properties were characterized by means of vector network analyzer ferromagnetic resonance spectroscopy (VNA-FMR). The samples were placed flip-chip onto a coplanar waveguide and the complex transmission parameter S_{21} was measured at constant frequency as the FMR signal, while the magnetic field was swept through resonance [51–54].

III. RESULTS AND DISCUSSION

A. Structural characterization

Figure 1 illustrates XRR scans in the range of $0.5^\circ \leqslant 2\theta \leqslant 8.0^\circ$ for the entire set of Co/Au samples, with the left inset showing the specific layer sequence that we used including all template layers. Interference-caused Kiessig fringes with two different periods are distinguishable in Fig. 1 for high N. The first type, with a period inversely proportional to N, can be observed at low 2θ values. These short-period oscillations correspond to the total thickness of the MLs, since by increasing N (i.e., the total sample thickness) the distance between two consecutive minima or maxima decreases. At the same time, their relative intensity decreases while increasing N, due to the increasing number of interfaces as well as due to the x-ray absorption in each individual layer. In a wider 2θ range, a second set of Kiessig fringes is noticeable, whose period ($\Delta\theta \approx 0.2^\circ$) is constant as a function of N. They originate from the 20-nm-thick Au buffer layer. More importantly, the development of first-, second-, and third-order Bragg-like superstructure peaks are observed with increasing N, giving a clear signature of a well-defined periodic elemental ML modulation. Fitting them to a Gaussian profile, the total thickness of the repeating Co/Au bilayer $t_{\mathrm{Co/Au}}$ was evaluated [55]. The right inset in Fig. 1(a) shows the N dependence of $t_{\mathrm{Co/Au}}$, where the error bars correspond to the standard deviation values. Under the assumption of a purely statistical Gaussian distribution for the observed $t_{\mathrm{Co/Au}}$ values, the data sets fall into the interval defined by $t_{\mathrm{Co/Au}} = 3.61 \pm 0.02$ nm, consistent with the nominal Co/Au bilayer thickness of 3.6 nm.

The XRR data for each of the films were further modeled in one group of layer segments, sandwiched between the Au seed and Au capping layers using the GENX software [56]. Instead of treating every multilayer repeat individually, we introduced segments in order to significantly reduce the number of parameters required for a reasonable fit. Each segment contains one Co/Au bilayer repeat. The thickness, density, and roughness of the Co and Au layers were each fitted to one respective value that in our model was used identically for the complete multilayer. The fitting results are shown in Fig. 1(a)

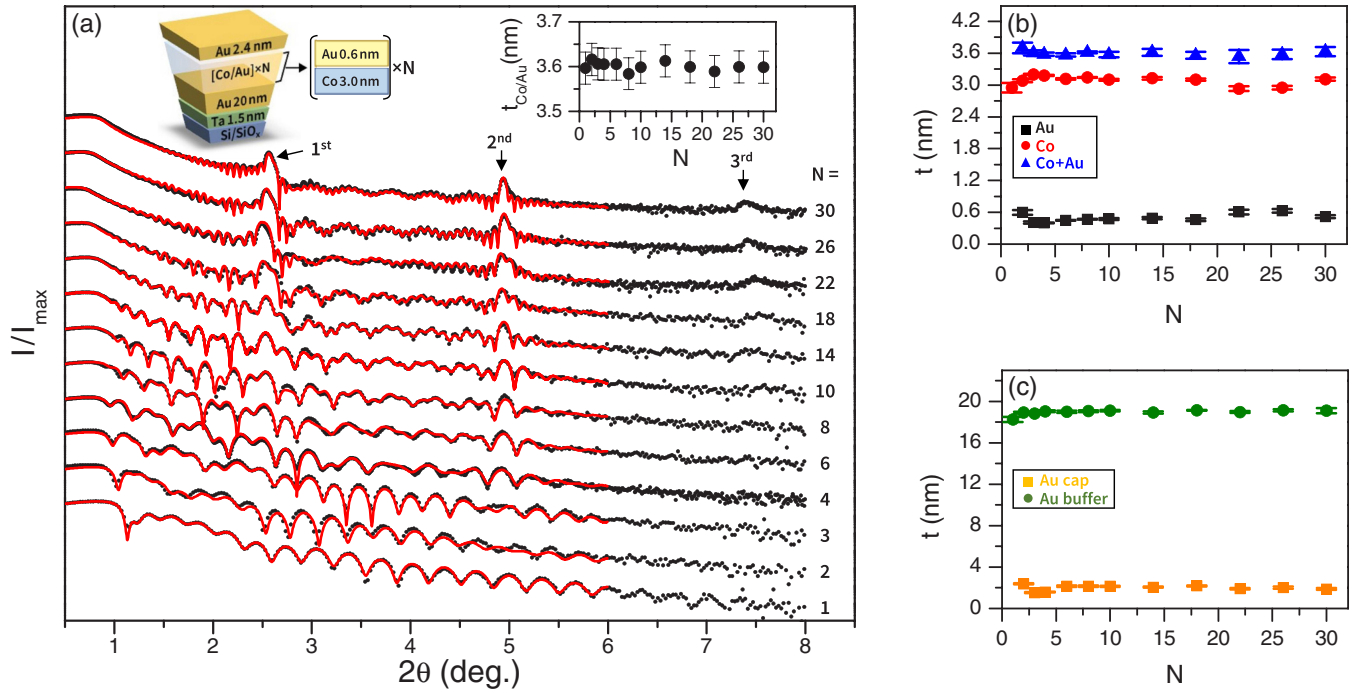

FIG. 1. (a) XRR scans of all $[Co(3.0\,nm)/Au(0.6\,nm)]_N$ multilayer samples. The (red) solid lines represent the least-squares fits obtained with the GENX software. The top-left inset shows a schematic drawing of the layer stack. The top right inset displays the average total thickness of the single Co/Au bilayer as a function of N as obtained from XRR measurements. (b) Determined thicknesses from the XRR data fit for the Au, Co, and their sum as (black) squares, (red) circles, and (blue) triangles, respectively. (c) Determined thicknesses from the XRR data fit for the Au cap and Au buffer layers as (orange) squares and (green) circles, respectively.

as (red) lines. From the data fit, we have determined the thicknesses for the Co and Au layers, both displayed in Fig. 1(b) together with their sum. The extracted values are very stable as a function of N around their nominal value, further confirming well-defined and reproducible periodic elemental ML modulation while increasing the total thickness. Figure 1(c) shows the determined thickness values for the Au cap and buffer layers, both being constant around their nominal values verifying the robustness of our fabrication process.

We were able to evaluate also the layer roughnesses by our fitting model, resulting (once averaged across all N) for the Co and Au layers in $\sigma_{Co} = 0.48 \pm 0.03$ nm and $\sigma_{Au} = 1.07 \pm 0.06$ nm, respectively, where the errors correspond to the standard deviation values. Although the low standard deviation indicates that the data points tend to be very close to their mean and therefore the interfaces quality is reproducible as a function of N, the absolute value for Au exceeds its thickness and may point to grossly incorrect fits. However, the XRR roughness values are a combination of two major contributions: the chemical one, describing the interdiffusion of the two neighboring layers, and the morphological one, influenced by layer thickness variations under the area illuminated by x rays. It is worth mentioning that our model considers interface boundaries that lie completely in the plane of the samples and that, as we will see further, our HRTEM images reveal on a very local scale negligible interdiffusion between Co and Au, i.e., chemical roughness is very small. The layer waviness and striations, which correspond to morphological roughness and which occur in our sample structures, as will be disclosed together with the TEM images, are responsible for the large evaluated roughness value of the Au interlayer.

Figure 2(a) shows the XRD scans in the full angular range $28^\circ \leqslant 2\theta \leqslant 102^\circ$ for all Co/Au samples. All the scans look very similar in their overall appearance, exhibiting only well-defined diffraction peaks corresponding to Si(400), Au(111), and Au(222) originating from the buffer layer. The superstructure reflections Co(0002)/Au(111) and Co(0004)/Au(222) are visible as well. In the following, they are abbreviated as Co/Au* and Co/Au**, respectively. Even though heteroepitaxial growth of crystalline layers is usually performed directly on top and facilitated by single crystalline substrates, the presence of a thermally oxidized SiO_x thick layer is not preventing the sputtered Au thin films from developing a highly oriented fcc (111) textured growth [42]. In fact, fcc metal films have the largest atomic packing density along the (111) crystal plane and thereby the lowest surface energy. Therefore, while using such materials as buffer layers, the sample architecture studied in this work could very well be transferred to a large variety of different substrates without losing the specific crystal quality. Moreover, the Au buffer layer peaks look virtually the same for all samples, both in terms of angular position and peak width, verifying the robustness of our fabrication process.

Hereby, the total angular x-ray scan range shows only well-defined fcc (*nnn*) and hcp (0002*l*) peaks for Au and Co, respectively. However, since our x-ray investigation is not able to exclude the presence of fcc stacking faults in Co, the hcp lattice of Co was additionally verified via in-plane diffraction

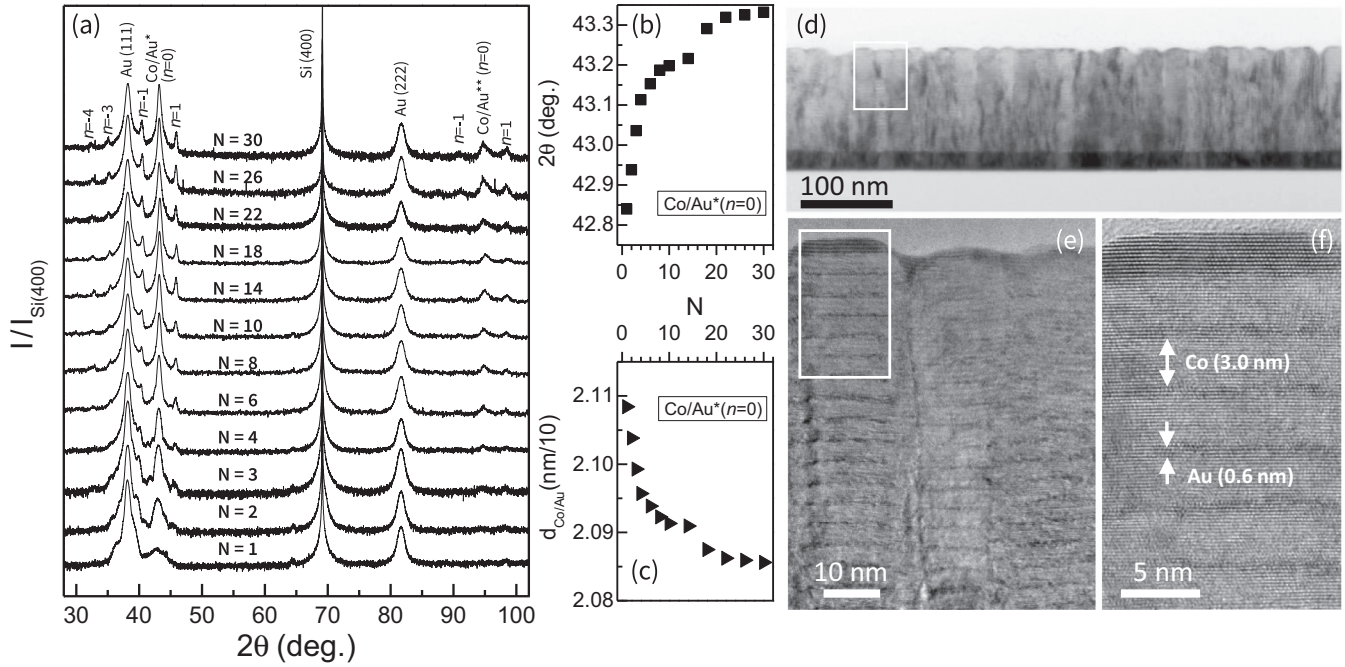

FIG. 2. (a) X-ray θ-2θ scans of all samples. Each scan has been normalized to the intensity of its Si (400) substrate peak. (b) shows the N dependence of the Co/Au* ($n = 0$) diffraction peak position (squares), while (c) displays the associated average out-of-plane interplanar distance $d_{\mathrm{Co/Au}}$ of the Co/Au heterostructure vs N. [(d)−(f)] Cross-sectional TEM image of the $[\mathrm{Co}(3.0\,\mathrm{nm})/\mathrm{Au}(0.6\,\mathrm{nm})]_{30}$ sample using different magnifications. The (white) rectangle in (d) shows the magnified area that is displayed in (e), whereas the (white) rectangle in (e) indicates the magnified area shown in (f).

measurements, by setting the incident and diffracted beams nearly parallel to the sample surface, in which only Co $(11\bar{2}0)$, Co$(10\bar{1}0)$, and Au(220) reflections were measured for our samples. Moreover, satellite reflections around the superstructure diffraction peaks [indexed by n in Fig. 2(a)] have been measured, which are a clear indication of a perpendicular structural coherence length far larger than the thickness of the individual constituent layers. It can be also observed that the negative indexed satellite diffraction peaks for the Co/Au samples have higher intensity than the positive ones, with the latter being within the noise level for $n > 1$. This effect, whose prominence being mainly appreciable for the first-order diffraction peaks, is mainly caused by the overlapping and interfering waves coming from the negatively indexed satellite diffractions and the Au(111) reflection.

Furthermore, the diffraction conditions for the Au(111) lattice planes occur at different angles, due to their different lattice dimensions resulting in $d_{111,\mathrm{Au}} = 0.236$ nm, compared to the volume-averaged interplanar spacing of the Co(3.0 nm)/Au(0.6 nm) bilayer, corresponding to $d_{\mathrm{Co/Au}*} = 0.208$ nm. This would lead to different magnitudes of strain throughout the ML structures depending on the number of times the Co/Au bilayer building block was repeated. Thus, one could anticipate that otherwise identically prepared and similar films of different thickness may have different depth-dependent strain profiles. As expected, the diffraction peak intensity for Co/Au* and Co/Au** increases as the total structure becomes thicker, simply due to the larger amount of epitaxial ordered material. Nevertheless, upon carefully analyzing their angular position as a function of N [Fig. 2(b)], a continuous shift to higher 2θ angles is found as N increases. This indicates that for small N the Co/Au bilayers are under larger tensile strain, which is partially being released as the growth progresses. For samples with a larger value of N, the thickness dependent strain relaxation becomes increasingly prominent, hereby approaching a bulklike lattice parameter value as shown in Fig. 2(c). This process is occurring within each sample via the internal relaxation of the lattice mismatch induced stress by the occurrence of misfit dislocations and lattice defects during growth, which would then propagate towards the Co/Au interfaces. One could also conclude that the dislocations are more numerous in the early stages of growth once they start to form, as the stress needed to relief is larger at this point as compared to the topmost extent of the larger N samples, where a significant part of the stress has already been released. From this point of view, it is reasonable to assume that the Co/Au ML samples possess a gradient of strain across their vertical extent. In spite of these considerations, the first- and second-order superstructure diffraction peaks for the Co/Au MLs occur at nearly the same angle for $N > 10$ repetitions, thus indicating that the total thickness at $N = 10$ nearly reached the critical thickness needed to relax the corresponding strains.

Moreover, it cannot be neglected that the presence of several interfaces due to the alternate deposition of FM/NM layers could influence the ML growth by inducing the formation of specific morphological features. Figs. 2(d)–2(f) show cross-sectional bright-field and high-resolution TEM images for $N = 30$. On the large-scale image in Fig. 2(d), both the intragrain buckling and an intergranular roughness due to very slight grain-to-grain variations in growth rate of the ML at its top can be appreciated. Without impacting the detectable

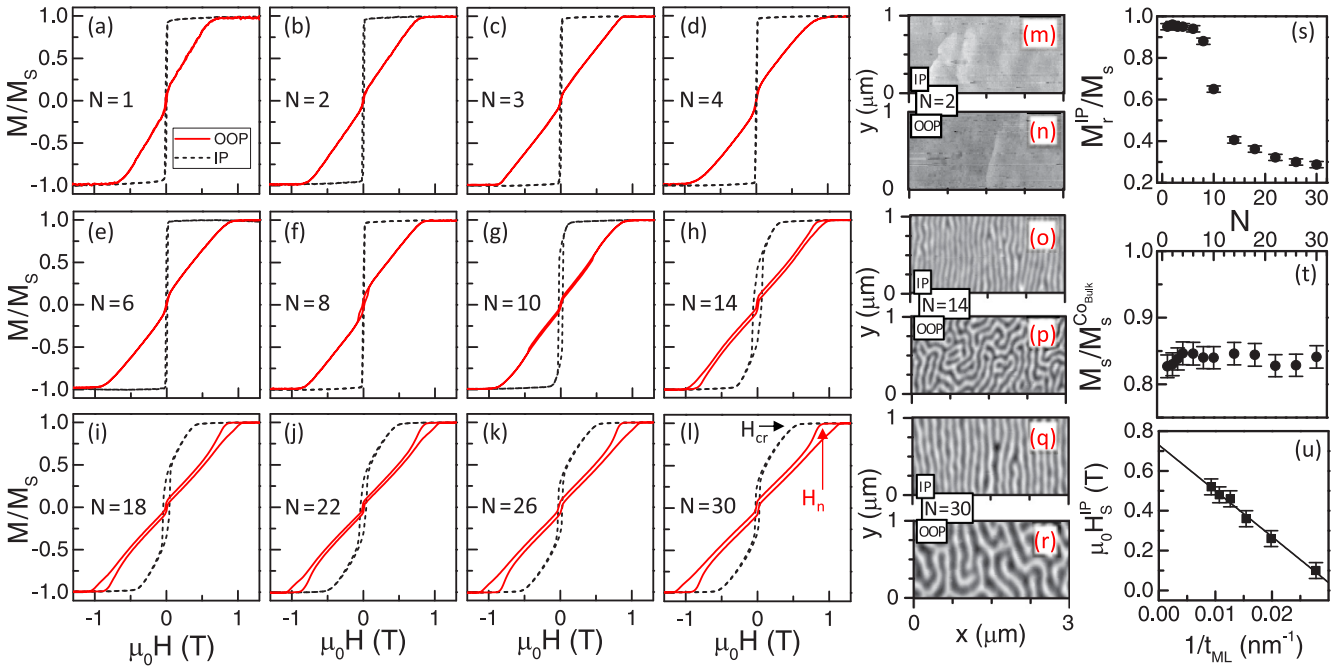

FIG. 3. [(a)−(l)] VSM room-temperature (RT) magnetization reversal curves with the applied field along the IP (black dashed lines) and OOP (red full lines) directions for the entire set of $[Co(3.0\,nm)/Au(0.6\,nm)]_N$ samples. Data are normalized to its M_S in each case. [(m)−(r)] Remanent MFM images recorded after IP [(m), (o), and (q)] and OOP [(n), (p), and (r)] demagnetization processes for the samples [(m) and (n)] $N = 2$, [(o) and (p)] 14, and [(q) and (r)] 30. (s) N dependence of the in-plane remanence ratio M_r^{IP}/M_S [obtained from the magnetometry data of (a)−(l)]. (t) RT saturation magnetization M_S as a function of the Co/Au bilayer repetitions N. (u) RT in-plane saturation field $\mu_0 H_s^{IP}$ as a function of the inverse total multilayer thickness $t_{ML} = N \times \Lambda$, with $\Lambda = 3.6$ nm being the Co/Au bilayer period. The solid line represents the least-squares fits to Eq. (1).

and well-defined crystallographic texture measured using x-rays, a columnar grain structure is clearly visible in Fig. 2(e) together with a precise and well-established layer structure. The columns are mostly extended throughout the whole thickness of the ML film and are largely perpendicular to the substrate with almost parallel grain boundaries. Cumulative layer waviness from grain to grain is also observed, as a result of shadowing effects inherent to the room-temperature sputtering process, of the heteroepitaxial growth initiated from the buffer layer and of the thickness discrepancy of the constituent layers in the ML [57,58]. Finally, the high-resolution image displayed in Fig. 2(f) clearly shows continuous Au interlayers within one grain and negligible intergranular chemical interdiffusion even near the top surface of the ML.

Thus both the observed strain relaxation and waviness can be regarded as important aspects related to the magnetodynamic properties of our samples, as will be discussed in Sec. III C. Hereby, our structural analysis confirms the good crystallographic quality of the optimized layer growth sequence resulting in well-modulated Co/Au MLs with perpendicular c-axis orientation, necessary for a preferential OOP orientation of the magnetization above a critical thickness [11–16].

B. Magnetostatic characterization

Figures 3(a)–3(l) present room-temperature normalized M/M_S data as a function of the field strength $\mu_0 H$ and number of Co/Au bilayer repetitions N, with M_S being the saturation magnetization. In each graph, the (black) short dashed and (red) solid lines show the magnetization reversal curves measured for an external magnetic field applied parallel and perpendicular to the film plane, respectively. Each sample with $14 \leqslant N \leqslant 30$ shows two reversal curves that are a clear indication of an OOP preferential orientation of magnetization [8,14,16,42].

For the IP field configuration, as one lowers the applied magnetic field, the saturated state becomes unstable at a critical field H_{cr} [pointed to in Fig. 3(l)] and undergoes laterally alternating magnetization rotations into a tilted stripe domain state driven by the magnetocrystalline OOP anisotropy [8,14,16,42]. For $0 < H < H_{cr}$, this tilted stripe domain state becomes the system ground state [59] and the precursor to perpendicular stripe domains at remanence. Its OOP magnetization modulation increases, and the IP magnetization decreases as the applied field is further reduced, which leads to the overall curved appearance of all the in-plane $M(H)$ measurements in Fig. 3 for $14 \leqslant N \leqslant 30$. However, a final IP magnetization component still persists at remanence due to Bloch-type domain walls that have been aligned during the field sequence into the in-plane external field direction and that are responsible for the IP hysteresis that occurs for low field values [14–16].

For the OOP field configuration instead, once the field is lowered, the uniform state is broken by the formation of bubble domains with opposite OOP magnetization orientation

driven by magnetostatic energy. This process starts rather abruptly at the nucleation field H_n^{OOP} [pointed out in Fig. 3(l)], leading to a sharp drop in the magnetization. As the field is further reduced, the domain dimensions increase to minimize the total magnetostatic energy resulting in the linear field dependence of the magnetization down to remanence [9,60,61]. Finally, one may associate the small hysteresis effect with interlayer exchange coupling effects. However, as the same effect is also visible in similar Co/Pt MLs [42], we attribute it to a nonuniform domain expansion and contraction around remanence, which is related to the existence of slight sample imperfections [14,16,42]. An appreciable change is noticeable as well in the two OOP-hysteretic regions at high field magnitudes, associated with the initial nucleation and final annihilation of domains. In fact, upon increasing N, i.e., the total thickness, their position along the magnetic field axis shifts to progressively higher values as well as their hysteretic area becomes gradually larger [14–16,42].

For the samples with $1 \leqslant N \leqslant 8$, despite the OOP orientation of the magnetocrystalline anisotropy axis, an IP behavior was found. For those samples the measurements show almost perfectly rectangular-shaped hysteresis loops for the IP applied field. In contrast, the OOP field data in Figs. 3(a)–3(f) show an almost completely reversible change in the magnetization orientation, where the complete alignment is reached only at a field strength of $\mu_0 H^{OOP} \approx \pm 1$ T.

Figure 3(g) shows the IP and OOP magnetization curves for the sample with $N = 10$. While the OOP curve shows the absence of high field nucleation hysteresis near saturation, the IP configuration demonstrates the persistence of a strong curvature of the loop and a very small remanent magnetization. Thus, the sample is evidently not in an IP magnetization state at remanence, meaning that it must undergo a perpendicular or tilted stripe domain reversal process if one lowers the externally applied field [30].

Finally, from our experimental data in Fig. 3, we concluded that N has a profound impact on the magnetization reversal characteristics of the $[Co(3\,nm)/Au(0.6\,nm)]_N$ MLs. The overall appearance of the IP and OOP magnetization reversal curves stays very similar for $14 \leqslant N \leqslant 30$ [Figs. 3(h)–3(l)]. However, while lowering the number of repetitions, thickness-induced magnetization reorientation transition takes place, which culminates with a reversal mechanism characterized by IP magnetization states alone [11,15,42].

In order to confirm the physical picture deduced from our VSM data, the remanent domain patterns were measured for three selected samples by MFM. For this purpose, the magnetic configuration was brought as close as possible to the equilibrium state in both the OOP and IP reference system by demagnetizing it, i.e., by applying an oscillating field of decreasing amplitude starting above the saturation magnetic field of each sample. Figures 3(m)–3(r) show MFM images for $[Co(3\,nm)/Au(0.6\,nm)]_N$ with $N =$ 2, 14, and 30. As expected, for samples with $N = 14$ and 30, the magnetic configuration consists of an array of perpendicular stripe domains with well-defined widths, which is disordered when the sample was previously OOP demagnetized [Figs. 3(p) and 3(r)] and is parallel aligned after IP demagnetization [Figs. 3(o) and 3(q)]. The MFM characterization shows also that the width of the remanent stripe domains decreases (increases) by decreasing (increasing) the total magnetic thickness in accordance with Kittel's law for stripe domains [12,15,42,62,65], spanning from 80 ± 8 nm ($N = 14$) to 122 ± 14 nm ($N = 30$) width. This demonstrates that the granularity of the films, which is on the order of ~20 nm as shown by the TEM images of Fig. 2, is much smaller and does not create significant lateral pinning sites. This observation is supported if we compare our MLs with samples in the existing literature, in which such pinning sites were purposely created by increasing the Ar sputter pressure for instance [63]. Finally, as the magnetization curves obtained for $N \leqslant 8$ are characteristic for a film with IP magnetization, the corresponding MFM images for $N = 2$ displayed in Figs. 3(m) and 3(n) show micrometer-size IP magnetic domains independently of the magnetic field orientation applied previously.

The transition from a remanent OOP stripe domain state (for $N \geqslant 14$) to a remanent uniform in-plane state (for $N \leqslant 8$) is mainly driven by the canting of the local magnetization [30]. Such canting angle varies monotonically with N as indicated by the N dependence of the IP remanence ratio M_r^{IP}/M_S shown in Fig. 3(s). Samples with $N > 14$ exhibit a low M_r^{IP}, arising mainly from the local magnetic moments confined inside the domain walls, which are parallel aligned during the IP field sequence and which are responsible for the remanent in plane magnetization. The IP remanence gradually increases when lowering N, indicating a canting of the domain magnetization towards the film plane. Finally, the ratio reaches values corresponding to a full IP remanent magnetization, thus confirming that the Co/Au samples (for $1 \leqslant N \leqslant 8$) are evidently in an IP-magnetized state at remanence.

The observed magnetic crossover from OOP to IP should be still correctly described by treating each ML as an effective single layer systems with the same saturation magnetization M_S, anisotropy K_u, and exchange stiffness A for each different total thickness [14,15,64–69]. We have determined the room-temperature saturation magnetization M_S for the entire set of samples with different N by taking into account the total magnetic thickness as $t_{ML} = N \times \Lambda$, with $\Lambda = 3.6$ nm being the Co/Au bilayer period. The results are plotted in Fig. 3(t) after having them normalized to the bulk value of the Co saturation magnetization of 1450 kA/m [70]. The data are showing that the ratios are nearly independent of N, i.e. the total thickness, with an average value of $\overline{M_S(Co/Au)/\,M_S^{Co_{bulk}}} = 0.84 \pm 0.01$. The stability of M_S and other magnetic parameters (see below) allows us to ascribe any significant change in the magnetic properties to the specific number of repetitions N as opposed to the inherent Co thickness variations or substantial CoAu alloying, which would both lead to substantial variation in the saturation magnetization.

Furthermore, the invariance of effective single layer magnetic parameters while changing N [15,68], can be also verified by the linear relationship between the IP saturation field $\mu_0 H_s^{IP}$ and the inverse of the total ML thickness t_{ML}:

$$\mu_0 H_s^{IP} = \frac{2K_u}{M_S} - \frac{2K_u}{M_S}\frac{1}{\sqrt{1+\frac{2K_u}{M_s^2}}}\frac{t_{cr}}{t_{ML}} \quad (1)$$

with t_{cr} being the critical thickness at which the reorientation transition occurs. In Fig. 3(u), we show the $\mu_0 H_s^{IP}$ experimen-

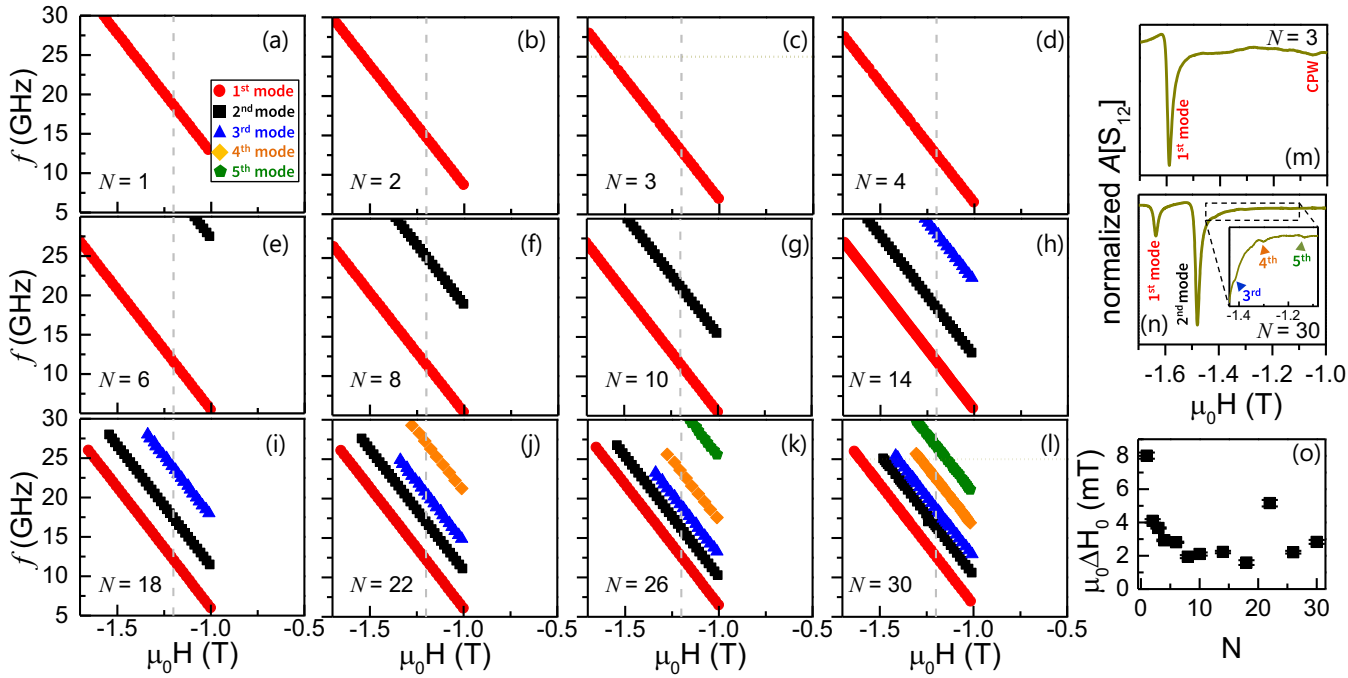

FIG. 4. [(a)−(l)] Frequency vs. magnetic field dependences of the ferromagnetic resonances for each sample. The external OOP magnetic field was always swept from −1.7 to −1 T, ensuring saturated OOP states through the whole measurement. The vertical dashed (gray) lines mark the value $\mu_0 H = -1.2$ T corresponding to the vertical cut that is used to construct Fig. 5, whereas the horizontal dotted (gold) lines in (c) and (l) correspond to the explicit measurements shown in (m) and (n). (m) and (n) show the normalized microwave absorption lines (amplitude of the S_{12} parameter) as a function of the applied field for the samples $N = 3$ and 30, respectively, which were measured with an excitation frequency of 25 GHz. (o) Contribution of the inhomogeneous broadening to the total field linewidth vs N.

tal data for $10 \leqslant N \leqslant 30$ as a function of $1/t_{\mathrm{ML}}$, excluding the samples that show already a preferential IP magnetization. All the data follow a linear trend and share a common intercept $2K_u/M_s = 0.73$ T. Furthermore, we have obtained $t_{\mathrm{cr}} = 41.4 \pm 1.8$ nm (approx. corresponding to $N = 12$), in agreement with the experimental data. It is worth emphasizing that the evaluated magnetic anisotropy is first integrated over the entire ML volume, thus the total-thickness dependent interface and magnetocrystalline anisotropies within each sample are averaged out. Secondly, they are averaged within $10 \leqslant N \leqslant 30$ by the linear fit itself.

Accordingly, despite the existence of magnetization magnitude modulations along the thickness, whose degree depends on the nonmagnetic material, all the samples behave as single-effective ferromagnetic layers with weak PMA under the application of external magnetic fields [14,16]. Nonetheless, all the OOP reversal curves are almost identical in the high-field regime. Therefore appreciable changes from sample to sample are not expected in terms of dynamic properties of their magnetization in the saturated state. However, as already shown in Fig. 2 and discussed in Sec. III A, the interface and magnetocrystalline anisotropy should be considered as thickness dependent due to the strain evolution within each ML sample along the thickness, which will be the focus of the following section.

C. FMR study

The FMR was measured using a VNA-based spectrometer in a field-sweep mode. For each field-sweep, a fixed microwave frequency in the range from 0 to 35 GHz was selected. As we have seen from the hysteresis curves in Fig. 3, a static OOP magnetic field of $\mu_0 H = \pm 1$ T is sufficient to keep the magnetization saturated for each sample in the normal direction. Therefore, to ensure that all measurements start and run in the same magnetic state, the magnetic field was always swept from $\mu_0 H = -1.7$ to -1 T. The FMR spectra were fitted with a complex Lorentzian function to retrieve the resonance fields.

Figures 4(a)–4(l) show the resonance frequencies as a function of the static external magnetic field for all samples (N) of our series. Since for $0 \leqslant f \leqslant 5$ GHz no resonance was detected, the y-axes are set from 5 to 30 GHz. Figure 4(a) shows the data of the thinnest sample in this study, i.e., $N = 1$ or Au(20 nm)/Co(3 nm)/Au(3 nm). Only one mode is visible in the explored frequency range, which corresponds to the uniform magnetization precession mode in the single Co layer characterized by a uniform dynamic magnetization across its thickness. At the other end of our sample series, Fig. 4(l) displays the frequency-field dependence of the thickest $N = 30$ sample. In this case, many modes are visible. The modes are always labeled from bottom to top, i.e. from lowest frequency (first mode, red dots) to highest frequency (fifth mode, green pentagons). As mentioned above for a uniform single layer material, the detected FMR mode may be associated with the uniform precession of the magnetization. However, as we will see in detail further, the ML nature of the samples introduces a more complex scenario with a distribution of FMR amplitudes along the structure. The higher-order modes (second to fifth) can be identified as "PSSW-like" along the ML thickness. The

observation of both odd and even modes implies that the mode amplitude profiles are asymmetric with respect to the sample thickness. Intriguingly, by decreasing the number of Co/Au repetitions from $N = 30$ backward, all the PSSW-like modes could still be excited at higher frequencies when the same static field is applied. Importantly, higher-order modes have not been measured for $N < 6$. This might erroneously suggest an apparent suppression due to the thickness-driven reorientation transition from OOP to IP preferential magnetization orientation. On the contrary, the absence of the higher-order responses at low N is associated to their shift in frequency into a range not accessible by our experimental setup (>35 GHz).

Moreover, the separation in frequency between modes increases with decreasing the total ML thickness, which could be understood on the basis of the perpendicularly quantized spin-wave vector being inversely proportional to the total film thickness. However, not only the PSSW-like modes are changing their resonance conditions upon changing N, but also the first mode. As already discussed in Sec. III B, magnetometry has revealed a magnetic crossover from OOP to IP as a function of the total thickness, with the samples $N \geqslant 10$ being correctly described with the same values of saturation magnetization M_S, anisotropy K_u, and exchange stiffness A. Nonetheless, those magnetic parameters were evaluated by an integral method (VSM) and XRD characterization has shown that the diffraction angle corresponding to the Co/Au superstructure Bragg peaks [displayed in Fig. 2(b)] shifts towards its bulk position with a steep increase between $1 \leqslant N \leqslant 10$. The angular position is directly related to the accommodation of misfits across any interface between Co and Au due to strain relaxation. This would correspond to an evolution of the interface quality as a function of N, which is dramatic for $N \leqslant 10$. This is therefore translated to the dynamic properties of such structures, as the first mode purely shows, given that it is not affected by total thickness effects. Indeed, for $N > 10$, a small change of the frequency positions of the first mode is still appreciable: despite corroborating that statically all these samples have the same structural properties and in particular the same Co and Au thicknesses, thus leading to nearly identical volume averaged magnetocrystalline and interface anisotropy fields, the dynamic response reveals the existence of small monotonic changes as N (and hence the total ML thickness) increases. We will argue that these changes originate in structural inhomogeneities (in particular, strain) along the vertical direction of the Co/Au ML stack.

Figures 4(m) and 4(n) show normalized absorption scans at a microwave frequency of $f = 25$ GHz for the samples $N = 3$ and 30, respectively, which correspond to the horizontal cut in Figs. 4(c) and 4(l) marked by the dotted (gold) lines. For the $N = 3$ sample, displayed in Fig. 4(m), only one mode is visible in the explored frequency range, which is characterized by a quasiuniform dynamic magnetization across its small thickness, along with the background signal originating from the coplanar waveguide (CPW) at $\mu_0 H = -1.05$ T. For the thickest sample, i.e., $N = 30$, the primary absorption peak at $\mu_0 H_{\text{res}} = -1.63$ T is accompanied by multiple modes appearing at lower applied magnetic fields, as shown in Fig. 4(n). One important mark is that the peak amplitude of the first mode is found to be smaller than the second mode, which may firstly appear to be counterintuitive. In fact by increasing N, i.e., the total magnetic thickness, one would expect an intensity increase of any resonance mode while maintaining the relative intensity hierarchy. However, as described in detail further, the amplitude profile of the first mode evolves dramatically as a function of N from being uniform (for very low N) towards exhibiting a monotonic distribution of amplitude along the thickness, converting itself into a surfacelike mode, mostly occupying the bottom region of the sample (for high N). Therefore, the first mode intensity saturates at a specific total thickness, whereas the second mode intensity continues to increase with increasing N.

Lastly, the inhomogeneous broadening $\mu_0 \Delta H_0\,(N)$ dependence [see Fig. 4(o)] for the first mode was extracted from the linewidth vs frequency plot [26,38,71], representing nonzero linewidth in the limit of zero frequency excitation. The $\mu_0 \Delta H_0$ values saturate at about $N = 10$, with the exception of $N = 22$, in agreement with the strain relaxation evolution that XRD data confirmed in the same total thickness range. Above $N = 10$, any further layer addition does not change the magnetic homogeneity dramatically, and the inhomogeneous damping evolution might serve as an additional indicator for structural and interface quality evolution of our samples. Actually, the Au interlayer roughness for the $N = 22$ sample, which was evaluated by fitting the XRR data, is higher than the ones of the other samples, contributing to the increased inhomogeneous scattering of the uniform precession mode, thus accounting for the increased damping for this sample, as seen in Fig. 4(o).

In order to model the investigated samples from a dynamic point of view, a more detailed approach has been applied with respect to the single effective layer model, which was sufficient to understand the thickness-dependent magnetization reorientation transition, but cannot explain the dynamic response. The model includes a bilinear interlayer exchange coupling throughout the Au interlayers, which is active just at the first nearest neighbors [72,73]. Thus, the interaction between two consecutive Co layers ν and η is given by

$$\epsilon_{\text{int}} = -J \frac{\mathbf{M}^{(\nu)} \cdot \mathbf{M}^{(\eta)}}{M_s^{(\nu)} M_s^{(\eta)}}, \tag{2}$$

where J is the interlayer exchange constant, with a value set to $J = 15\,\text{mJ/m}^2$ for all the investigated samples when fitting the data in Fig. 5. Although it is not necessary to understand the static properties of the investigated MLs, here the model includes surface anisotropies that are known to be induced by any Au/Co interface [74,75]. For the two outer Co layers (top-most and bottom-most), the effective anisotropy field is denoted by H_a^o, while H_a corresponds to the effective anisotropy field of the inner Co layers. Both surface anisotropies and interlayer exchange interaction are introduced as bulk energies, which are confined within the magnetic sublayers located next to the top and/or bottom surfaces [76–78]. Moreover, given that we are interested in the OOP saturated regime promoted by sufficient external magnetic field, we assume that the equilibrium magnetization of all layers is pointing along the normal axis. The time evolution of the magnetization is determined by the Landau–Lifshitz (LL) equation of motion [43], namely,

$$\dot{\mathbf{M}}^{(\nu)}(\mathbf{r}, t) = -\mu_0 \gamma \mathbf{M}^{(\nu)}(\mathbf{r}, t) \times \mathbf{H}^{e(\nu)}(\mathbf{r}, t). \tag{3}$$

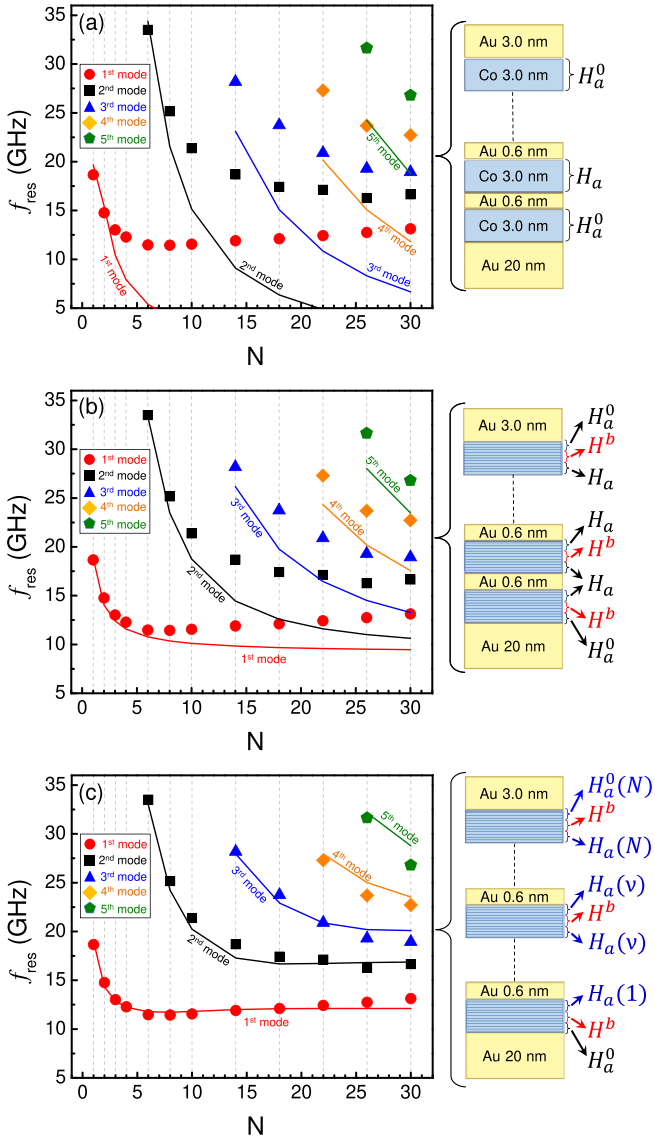

FIG. 5. [(a)–(c)] FMR measurements (dots) and theory (lines) evaluated at $\mu_0 H = -1.2$ T. Cases (a)–(c) show different approximations of the theoretical model (see text for details) that are summarized by the layer sketches on the right.

Here, the dot denotes the time derivative, γ is the absolute value of the gyromagnetic ratio, $\mathbf{M}^{(\nu)}(\mathbf{r},t)$ is the magnetization, and $\mathbf{H}^{e(\nu)}(\mathbf{r},t)$ is the effective field of the Co layer ν, respectively. In the linear approximation, both the magnetization and the effective field are written as $\mathbf{M}^{(\nu)}(\mathbf{r},t) = M_s^{(\nu)}\hat{z} + \mathbf{m}^{(\nu)}(\mathbf{r},t)$ and $\mathbf{H}^{e(\nu)}(\mathbf{r},t) = \mathbf{H}^{e0(\nu)} + \mathbf{h}^{e(\nu)}(\mathbf{r},t)$. Note that the z axis is aligned parallel to the normal axis, which corresponds to the equilibrium direction. In terms of the magnetization components, the LL equations of motion are

$$i\,\frac{\omega}{\mu_0\gamma} m_x^{(\nu)} = -m_y^{(\nu)} H_z^{e0(\nu)} + M_s^{(\nu)} h_y^{e(\nu)}, \tag{4}$$

$$i\,\frac{\omega}{\mu_0\gamma} m_y^{(\nu)} = m_x^{(\nu)} H_z^{e0(\nu)} - M_s^{(\nu)} h_x^{e(\nu)}, \tag{5}$$

where we assumed $\mathbf{m}^{(\nu)}(t) = \mathbf{m}^{(\nu)} e^{i\omega t}$ with $\omega = 2\pi f$, where f is the frequency. The spatial dependence of the magnetization has been omitted, since we are interested in the ferromagnetic resonance response, so that the wavelength of the spin waves is supposed to be very large and hence a coherent IP motion of the magnetic moments is expected in each Co layer. Now, the static z component of the effective field is

$$H_z^{e0(\nu)} = H + H_a^{(\nu)} - M_s^{(\nu)} + \sum_\eta \left(d\mu_0 M_s^{(\nu)}\right)^{-1} \times J(\delta_{\nu-1}\delta_\eta + \delta_{\nu+1}\delta_\eta), \tag{6}$$

where H is the external field, $H_a^{(\nu)}$ is the effective anisotropy field (encompassing surface magnetic anisotropy and magnetocrystalline anisotropy contributions, $H_a^{(\nu)} = (H_K^{(\nu)} + H_S^{(\nu)})$), $M_s^{(\nu)}$ is the demagnetizing field of the uniform state, d is the thickness of the ν-th Co layer (3 nm) and $\delta_{i,j}$ is the Kronecker delta function (0 if $i \neq j$ and 1 if $i = j$). The latter function indicates that the interlayer exchange coupling [see Eq. (2)] is approximated to be active on the next nearest neighbors only. On the other hand, the dynamic components of the effective fields are

$$h_{x,y}^{e(\nu)} = \sum_\eta \left(d\mu_0 M_s^{(\nu)} M_s^{(\eta)}\right)^{-1} J m_{x,y}^{(\eta)} (\delta_{\nu-1}\delta_\eta + \delta_{\nu+1}\delta_\eta). \tag{7}$$

By inserting Eqs. (6) and (7) into Eqs. (4) and (5), the system can be solved numerically.

Figure 5 shows a direct comparison of FMR experimental data (dots) and theory (lines) evaluated at $\mu_0 H^{\rm OOP} = -1.2$ T (saturated regime for any N), where the external field is applied normal to the sample. A systematic analysis was performed from the theoretical point of view to reach a good agreement with the FMR data and to justify the use of the proposed model. Typically, FMR is modeled under the assumption that the measured signal is coherent, i.e., the spatial extent of OOP features is small enough that the absorption corresponds to a single average OOP sample structure. By following this line of action, first we use a simple macrospin model to fit the experimental data [see Fig. 5(a)], where each Co layer has the same effective anisotropy field $\mu_0 H_a$ that is set by fitting the frequency of the first mode for $N = 1$. The outer layers have a different effective anisotropy field $\mu_0 H_a^o$ to take into account the effect of having a single neighboring exchange coupled layer. Here, with a macrospin we do not refer to a single macrospin for the entire sample structure, but instead each individual Co layer acts as a macrospin that is interlayer exchange coupled to the first nearest neighbor Co layers.

However, the attempt to model the FMR data with this simple macrospin model results in an incorrect fit, as shown in Fig. 5(a). Still, we observe that the model could be useful to explain the behavior of the low-frequency mode (red dots) for the cases of one, two or three Co layers ($N = 1$, 2, 3) since a reasonable agreement with the experimental results is obtained. Nevertheless, if N increases it is not possible anymore to find a good agreement between the FMR data and the theoretical calculation implying that such a simple macrospin model is not able to capture all the details of the dynamic magnetization for larger N values. Moreover, this

first simple approach considers the surface anisotropy fields to be weak within the effective field $\mu_0 H_a$ of the entire 3-nm-thick Co layer in the LL equation of motion, namely they are not assumed as located solely at the Co/Au interfaces.

In order to consider the variations of the dynamic magnetization along the thickness and the interfacially confined nature of the surface anisotropy fields, we use an approach that subdivides the FM layers [78], so that $\boldsymbol{m}^{(\nu)}$ varies along the $d = 3$ nm thick individual Co layer. Here, we define the anisotropy field $\mu_0 H_a$ uniquely within the sublayers that are next to the Au/Co interfaces, where both magnetocrystalline and surface anisotropy contributions are acting, while for the central region of the FM layer a different bulk anisotropy field parameter ($\mu_0 H^b$) is considered. This latter term originates mainly from the magnetocrystalline anisotropy, being enabled by the crystalline orientation of the ML stack as confirmed by the x-ray characterization and magnetometry measurements. Since the surface anisotropy is known to act solely at the interfaces of the FM/NM stack, we assume the magnetocrystalline anisotropy dominates over the surface anisotropy in the central 3-nm-thick Co film region. This case is shown in Fig. 5(b) and the adjacent sketch, where each individual FM layer is subdivided into 12 discrete sublayers indexed *SL*, which are FM coupled via an exchange stiffness constant $A = 28$ pJ/m equal for all the samples [79]. Twelve sublayers is the best compromise between accuracy of the fitting procedure and optimization of the computational time. Thus sublayers $SL = 1{-}4$ and 9–12 possess an effective field $\mu_0 H_a$, whereas the inner sublayers $5 \leqslant SL \leqslant 8$ are dominated by the effective field $\mu_0 H^b$ of magnetocrystalline origin. Once again, the effective fields of the sublayers adjacent to the bottom-most and top-most Co/Au interfaces are represented by a distinct fit parameter $\mu_0 H_a^o$, to account for the distinct boundary conditions. The agreement between the calculations (lines) and the experimental data (symbols) improves in general and substantially for repetition numbers up to $N = 6$ but fails to reproduce the FMR modes for samples with $N > 6$.

Overall, we noted that for both models the theoretical results always underestimate the experimentally determined FMR frequencies for high *N*. To account for this effect, we further include a variation of the anisotropy field as a function of the repeating Co film unit within the ML samples, such that the magnetic anisotropy field varies as we move from the bottom Co layer ($\nu = 1$) towards the topmost Co layer ($\nu = N$).

This type of modeling is challenging, as without significant constraints on the individual magnetic profiles, the number of free parameters can become prohibitively large, rendering the results meaningless. Thus we have chosen to build the model based on useful information already determined from the previously discussed magnetometry characterization as well as fitting the entire FMR data set with the same set of fitting parameters. This case is illustrated in Fig. 5(c), where a very good agreement between experiment (symbols) and calculation (straight lines) is finally achieved.

Figure 6 shows in detail the fitted values for the model depicted in Fig. 5(c). For the inner sublayers of the Co films ($5 \leqslant \mathrm{SL} \leqslant 8$), the anisotropy field was fixed to $\mu_0 H^b = 0.5$ T [80], whereas we allowed the interfacial sublayer anisotropy

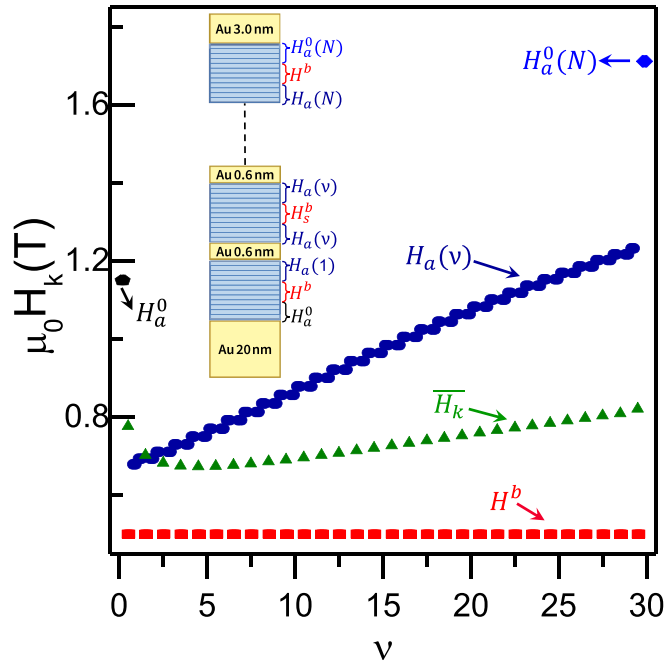

FIG. 6. Anisotropy fields as a function of ν for a sample with *N* Co/Au bilayers ($1 \leqslant \nu \leqslant N$). The bulk ($H^b$, red squares) as well as the bottom-most and top-most sublayer anisotropy fields (H_a^o, black pentagon and $H_a^o(N)$, light blue rhomb) are assumed fixed, while the anisotropy field at the boundaries of the inner Co layers [$H_a(\nu)$, dark blue dots] increases as its location moves towards the top part of the multilayers stack. The overall average anisotropy fields $\overline{H_K}(\nu)$ are shown as green triangles. The inset associates each anisotropy field to the corresponding region within the sample.

field ($SL = 1{-}4$, $9{-}12$) to vary from one Co layer to another, as $\mu_0 H_a(\nu)$. In addition, the anisotropy fields of the bottom-most and top-most sublayers adjacent to the Co/Au interfaces are allowed to have different specific values, which were determined from the fit to the $N = 1$ sample, thus obtaining $\mu_0 H_a^0 = 1.15$ T and $\mu_0 H_a^0(30) = 1.70$ T, respectively. We justify such different values by the magnetic polarization of Au that is expected to be strong for a thin Au layer and weak for a thick Au layer, which would lead to a larger reduction in M_S at the Au(20 nm)/Co(3 nm) bottom and Co(3 nm)/Au(3 nm) top interfaces as compared to all the inner Co/Au and Au/Co interfaces [81,82], thus causing an increase in the anisotropy fields localized at the outermost interfaces. It is worth highlighting that in our model the reduced M_S is solely affecting a third of the Co bottom and the Co top layers, i.e., four sublayers. Once averaged over the 12 sublayers, this reduction corresponds to 5% once compared to the average M_S value of the other Co layers, a sufficiently small difference that normally cannot be detected by our VSM integral method.

As can be seen in Fig. 6, the variable anisotropy field $\mu_0 H_a(\nu)$ increases with the Co layer number ν when moving from the bottom part of the ML stack upwards, while its slope becomes smaller by increasing ν. If we consider the obtained anisotropy values for $10 \leqslant \nu \leqslant 30$, we nicely find that the average value of the total uniaxial anisotropy field is $\mu_0 \overline{\overline{H_k}} = 0.75 \pm 0.04$ T, in good agreement with $2K_u/M_s = 0.73$ T that

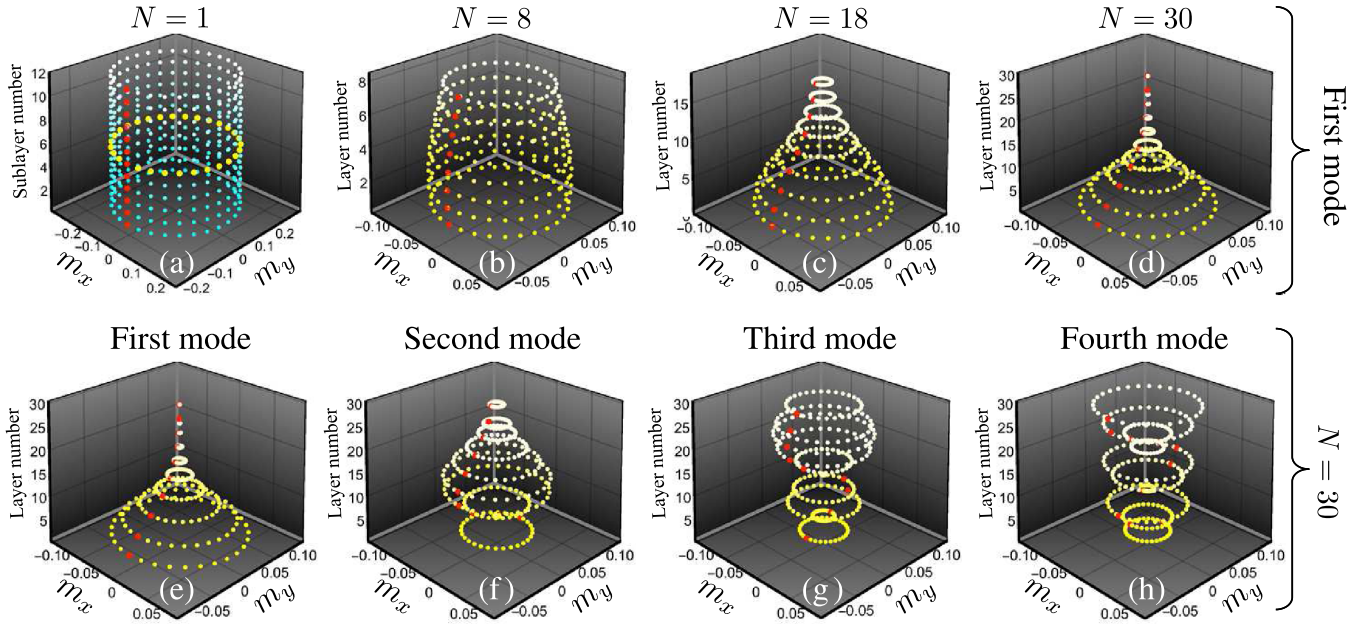

FIG. 7. In-plane dynamic magnetization orbits in z direction across the sample thickness as a function of N. In cases (a)–(d) the first mode is illustrated for different N values, while the first four excited modes are shown in (e)–(h) for the case $N = 30$. Dynamic magnetization components $m_{x,y}$ are expressed in arbitrary units. The red dots mark the excitation amplitude and phase for all modes at the same time ($t = 0$).

was evaluated from VSM data using the simple model of Fig. 3(u) and Eq. (1).

The vertical gradient in the anisotropy field term $\mu_0 H_a(\nu)$, is explained in terms of the growth induced strain relaxation process we found when analyzing the XRD data [83,84]. As subsequent Co/Au bilayers are grown, the introduction of misfit dislocations relieves the stress accumulated due to the mismatch of the Co/Au stack with the Au(111) buffer layer. It is also natural to assume that as more Co/Au bilayers are grown, the stress that builds up gradually attenuates. In fact, we found that most of the strain relaxation occurs upon growth of the first ten Co/Au bilayers [see Fig. 2(b)]. Thus, the density of the aforementioned misfit dislocations would naturally decrease when going from the Co/Au interfaces located in the bottom part of the ML stack towards the top-most interfaces.

It has been reported that misfit dislocations at interfaces in hcp Co films often consist of fcc-like inclusions, thus locally impacting the magnetocrystalline anisotropy energy of Co films due to the lower anisotropy of the fcc-like ordering as compared to hcp [85–87]. Thus we can now connect the gradient in the magnetic anisotropy field obtained from the fit to the dynamic model with a gradient in the concentration of misfit dislocations at the Co/Au interfaces. In the bottom region of the multilayer stack, a larger number of dislocations appears due to the larger stress build-up, which then effectively lowers the magnetocrystalline anisotropy contribution to the $\mu_0 H_a(\nu)$ term. As growth progresses and strain is gradually released, fewer dislocations are introduced, and thus, the magnetocrystalline anisotropy term to $\mu_0 H_a(\nu)$ being less affected by the presence of fcc-like inclusions in the interfacial region, such that a larger magnetic anisotropy develops towards the top region of the Co/Au ML stack.

It is interesting to consider that a variation of $\mu_0 H_a(\nu)$ along the vertical direction of the ML stack could also originate from a different surface anisotropy contribution as we go from one Co/Au interface to another along the vertical direction. In fact, the surface waviness observed in the TEM micrograph in Figs. 2(d)–2(f) might suggest that the surface anisotropy is influenced by the nonideal, wavy interface geometry. TEM imaging does not show, however, a clear gradient of the waviness when moving from the bottom-most to the top-most part of the stacks, such that we associate the main contribution to the anisotropy field gradient from a perspective of strain relaxation induced magnetocrystalline anisotropy reduction by the presence of dislocations.

The proposed model also allows for evaluating the depth profile of the dynamic response amplitude. The corresponding dynamic magnetization profiles are shown in Fig. 7. In Fig. 7(a), the case of one isolated FM layer ($N = 1$) is shown where the orbits of the sublayers are depicted. The red dots denote the $t = 0$ point, i.e., they mark the excitation amplitude and phase for all modes at the same time, while the orbit highlighted with yellow thick dots corresponds to the orbit of the 7-th sublayer. As the number of layers increases, the orbits change radically as depicted in Figs. 7(b)–7(d), introducing an amplitude distribution throughout the layers while keeping them in phase. Due to the different anisotropies at the top and bottom parts of the ML, the higher amplitude is mainly located at the bottom part of the structure, where the local anisotropies are smaller. This behavior explains why the first mode (or low-frequency mode) does not significantly change at higher values of N. Indeed, by increasing N the first mode becomes gradually a mode that is confined at the bottom part of the sample. The excited mode profiles for $N = 30$ are illustrated in Figs. 7(e) and 7(f), which are showing the nonmonotonic amplitude profiles of the high-order modes, whose distribution depends on the energy profile along the total thickness.

For high mode numbers, the phase changes by 180°, giving them a spin-wave character. Therefore, a PSSW-like mode

in thinner ML films needs dramatically more energy, due to higher exchange energy needed for the same kind of wave.

IV. CONCLUSIONS

In this paper, we have successfully fabricated $[Co(3.0\,nm)/Au(0.6\,nm)]_N$ multilayer films with a magnetic anisotropy axis perpendicular to the ML plane. The RT magnetometry measurements for the samples with $N > 10$ reveal two very different magnetization reversal processes for external applied fields within and perpendicular to the film plane: namely (i) an instability-driven reversal process leading to the generation of parallel stripe domains for IP field orientation and (ii) a domain nucleation process that is hysteretic in nature for OOP field orientation [42]. Our N-dependent study shows a gradual shrinking of the nucleation regime with decreasing N, so that at sufficiently low N only the instability-driven second-order phase transition occurs even for OOP-applied fields. The disappearance of the nucleation regime is driven by the strongly thickness-dependent balance between magnetic anisotropy and magnetostatic energies and occurs before the effective OOP anisotropy energy becomes too weak to support a stripe domain state altogether, i.e., it occurs while the stripe domain instability is still dominating the magnetization reversal process by spontaneously forming stripe domains at a critical applied field without a real bubble nucleation and stripe propagation process. By further reducing the number of Co/Au repetitions below $N < 10$, we observe a characteristic in-plane easy-plane magnetic behavior.

Moreover, we have demonstrated that such MLs provide an efficient platform for the excitation of PSSWs, whose characteristics turn out to be strongly dependent on the material modulation along the total thickness induced by the multilayering itself. Specifically, we identify various dynamic excitations for statically OOP saturated multilayer state, which are excited under rf fields. Therefore, in contrast to homogeneous thick films or thin multilayer systems, the investigated structures allow for a full comprehension of the conversion of periodic material and magnetic properties along the sample stack into a vertical array of exchange-based pinning planes for the PSSW modes within the film. In this context, in particular the decreased exchange across the Au interlayers seems to be responsible for the more complex dynamic behavior, as compared to systems with a less strong vertical exchange modulation, such as, for example, in typically investigated Co/Pt and Co/Pd ML systems. Moreover, we demonstrate that PSSW modes provide a handle to study the magnetic interactions and their modulation along the thickness in such ML systems, offering a unique platform for full tunability of the mode frequencies and amplitude profiles. Our observations can be generalized for different multilayered ferromagnetic materials exhibiting OOP preferential orientation of magnetization. Overall, our work illustrates the substantial relevance of PMA thin films for a very detailed understanding of high-frequency spin wave excitations in artificially multilayered systems.

ACKNOWLEDGMENTS

L.F. is very thankful to K. Potzger for the support with experimental facilities and to Ruslan Salikhov for his help with the AFM/MFM characterization. The authors thank R. Aniol for TEM specimen preparation. R.A.G. acknowledges the financial support from Fondecyt Iniciación, Grant No. 11170736 and Basal Program for Centers of Excellence, Grant No. FB0807 CEDENNA, CONICYT. CzechNanoLab Project No. LM2018110 funded by MEYS CR is gratefully acknowledged for supporting the experimental work at CEITEC Nano Research Infrastructure. This work has received funding from the European Union's Horizon 2020 research and innovation program under the Marie Skłodowska-Curie Actions and it is co-financed by the South Moravian Region under Grant Agreement No. 665860. The use of the HZDR Ion Beam Center TEM facilities is gratefully acknowledged.

[1] M. N. Baibich, J. M. Broto, A. Fert, F. Nguyen Van Dau, F. Petroff, P. Etienne, G. Creuzet, A. Friederich, and J. Chazelas, Phys. Rev. Lett. **61**, 2472 (1988).

[2] P. M. Levy, S. Zhang, and A. Fert, Phys. Rev. Lett. **65**, 1643 (1990).

[3] M. T. Johnson, P. J. H. Bloemen, F. J. A. den Broeder, and J. J. de Vries, Rep. Prog. Phys. **59**, 1409 (1996).

[4] P. F. Carcia, A. D. Meinhaldt, and A. Suna, Appl. Phys. Lett. **47**, 178 (1985).

[5] W. B. Zeper, F. J. A. M. Greidanus. P. F. Carcia, and C. R. Fincher, J. Appl. Phys. **65**, 4971 (1989).

[6] C. J. Lin, G. L. Gorman, C. H. Lee, R. F. C. Farrow, E. E. Marinero, H. V. Do, H. Notarys, and C. J. Chien, J. Magn. Magn. Mater. **93**, 194 (1991).

[7] D. Weller, W. Reim, K. Spörl, and H. Brändle, J. Magn. Magn. Mater. **93**, 183 (1991).

[8] O. Hellwig, A. Berger, J. B. Kortright, and E. E. Fullerton, J. Magn. Magn. Mat. **319**, 13 (2004).

[9] J. E. Davies, O. Hellwig, E. E. Fullerton, G. Denbeaux, J. B. Kortright, and K. Liu, Phys. Rev. B **70**, 224434 (2004).

[10] R. Sbiaa, Z. Bilin, M. Ranjbar, H. K. Tan, S. J. Wong, S. N. Piramanayagam, and T. C. Chong, J. Appl. Phys. **107**, 103901 (2010).

[11] C. Kittel, Rev. Mod. Phys. **21**, 541 (1949); C. Kittel, and J. K. Galt, Solid State Phys. **3**, 437 (1956).

[12] A. Hubert and R. Schäfer, *Magnetic Domains* (Springer-Verlag, Berlin Heidelberg, 1998).

[13] S. S. P. Parkin, H. Hopster, J- P. Renard, T. Shinjo, and W. Zinn, *Magnetic Surfaces, Thin Films, and Multilayers, MRS Symposia Proceedings No. 231* (Materials Research Society, Pittsburgh, 1992).

[14] M. Hehn, S. Padovani, K. Ounadjela, and J. P. Bucher, Phys. Rev. B **54**, 3428 (1996).

[15] E. Sallica Leva, R. C. Valente, F. Martínez Tabares, M. Vásquez Mansilla, S. Roshdestwensky, and A. Butera, Phys. Rev. B **82**, 144410 (2010).

[16] L. Fallarino, O. Hovorka, and A. Berger, Phys. Rev. B **94**, 064408 (2016).

[17] T. G. Phillips and H. M. Rosenberg, Rep. Prog. Phys. **29**, 285 (1966).

[18] S. E. Barnes, Adv. Phys. **30**, 801 (1981).

[19] Z. Frait and D. Fraitova, in *Spin Waves and Magnetic Excitations*, edited by A. S. Borovik-Romanov and S. K. Sinha (Elsevier, Amsterdam, 1988), Vol. 2.

[20] B. Heinrich and J. F. Cochran, Adv. Phys. **42**, 523 (1993).

[21] Z. Celinski, K. B. Urquhart, and B. Heinrich, J. Magn. Magn. Mater. **166**, 6 (1997).

[22] M. Farle, Rep. Prog. Phys. **61**, 755 (1998).

[23] G. Srinivasan and A. N. Slavin, *High Frequency Processes in Magnetic Materials* (World Scientific, River Edge, New Jersey, 1994); P. E. Wigen, and C. E. Patton, Phys. Rep. **103**, 251 (1984).

[24] Y. V. Khivintsev, L. Reisman, J. Lovejoy, R. Adam, C. M. Schneider, R. E. Camley, and Z. J. Celinski, J. Appl. Phys. **108**, 023907 (2010).

[25] K. J. Kennewell, M. Kostylev, N. Ross, R. Magaraggia, R. L. Stamps, M. Ali, A. A. Stashkevich, D. Greig, and B. J. Hickey, J. Appl. Phys. **108**, 073917 (2010).

[26] M. A. W. Schoen, J. M. Shaw, H. T. Nembach, M. Weiler, and T. J. Silva, Phys. Rev. B **92**, 184417 (2015).

[27] H. Qin, S. J. Hämäläinen, and S. van Dijken, Sci. Rep. **8**, 5755 (2018).

[28] F. Schreiber and Z. Frait, Phys. Rev. B **54**, 6473 (1996).

[29] R. Magaraggia, K. Kennewell, M. Kostylev, R. L. Stamps, M. Ali, D. Greig, B. J. Hickey, and C. H. Marrows, Phys. Rev. B **83**, 054405 (2011).

[30] A. Conca, E. Th. Papaioannou, S. Klingler, J. Greser, T. Sebastian, B. Leven, J. Losch, and B. Hillebrands, Appl. Phys. Lett. **104**, 182407 (2014).

[31] S. Klingler, A. V. Chumak, T. Mewes, B. Khodadadi, C. Mewes, C. Dubs, O. Surzhenko, B. Hillebrands, and A. Conca, J. Phys. D: Appl. Phys. **48**, 015001 (2015).

[32] F. Busse, M. Mansurova, B. Lenk, M. von der Ehe, and M. A. Münzenberg, Sci. Rep. **5**, 12824 (2015).

[33] I. Razdolski, A. Alekhin, N. Ilin, J. P. Meyburg, V. Roddatis, D. Diesing, U. Bovensiepen, and A. Melnikov, Nat. Commun. **8**, 15007 (2017).

[34] A. Navabi, C. Chen, A. Barra, M. Yazdani, G. Yu, M. Montazeri, M. Aldosary, J. Li, K. Wong, Q. Hu, J. Shi, G. P. Carman, A. E. Sepulveda, P. Khalili Amiri, and K. L. Wang, Phys. Rev. Appl. **7**, 034027 (2017).

[35] A. Haldar, C. Banerjee, P. Laha, and A. Barman, J. Appl. Phys. **115**, 133901 (2014).

[36] H. S. Song, K. D. Lee, C. Y. You, S. H. Yang, S. Parkin, B. G. Park, J. W. Sohn, J. Il Hong, and S. C. Shin, Appl. Phys. Express **8**, 053002 (2015).

[37] C. Bilzer, T. Devolder, J.-V. Kim, G. Counil, C. Chappert, S. Cardoso, and P. P. Freitas, J. Appl. Phys. **100**, 053903 (2006).

[38] D. B. Gopman, J. W. Lau, K. P. Mohanchandra, K. Wetzlar, and G. P. Carman, Phys. Rev. B **93**, 064425 (2016).

[39] T. Seki, K. Utsumiya, Y. Nozaki, H. Imamura, and K. Takanashi, Nat. Commun. **4**, 1726 (2013).

[40] J. Walowski and M. Münzenberg, J. Appl. Phys. **120**, 140901 (2016).

[41] A. El-Ghazalya, J. Gorchon, R. B. Wilson, A. Pattabi, and J. Bokor, J. Magn. Magn. Matter. **502**, 166478 (2020).

[42] L. Fallarino, A. Oelschlägel, J. A. Arregi, A. Bashkatov, F. Samad, B. Böhm, K. Chesnel, and O. Hellwig, Phys. Rev. B **99**, 024431 (2019).

[43] M. Lakshmanan, Philos. Trans. R. Soc. A **369**, 1280 (2011).

[44] W. Jiang, G. Chen, K. Liu, J. Zang, S. G. E. te Velthuis, and A. Hoffmann, Phys. Rep. **704**, 1 (2017).

[45] V. Kashid, T. Schena, B. Zimmermann, Y. Mokrousov, S. Blügel, V. Shah, and H. G. Salunke, Phys. Rev. B **90**, 054412 (2014).

[46] H. Yang, A. Thiaville, S. Rohart, A. Fert, and M. Chshiev, Phys. Rev. Lett. **115**, 267210 (2015).

[47] P. Bruno and C. Chappert, Phys. Rev. Lett. **67**, 1602 (1991).

[48] V. Grolier, D. Renard, B. Bartenlian, P. Beauvillain, C. Chappert, C. Dupas, J. Ferre, M. Galtier, E. Kolb, M. Mulloy, J. P. Renard, and P. Veillet, Phys. Rev. Lett. **71**, 3023 (1993).

[49] A. Bounouh, P. Beauvillain, P. Bruno, C. Chappert, R. Mégy, and P. Veillet, Europhys. Lett. **33**, 315 (1996).

[50] M. Matczak, B. Szymanski, M. Urbaniak, M. Nowicki, H. Głowinski, P. Kuswik, M. Schmidt, J. Aleksiejew, J. Dubowik, and F. Stobiecki, J. Appl. Phys. **114**, 093911 (2013).

[51] Y. Ding, T. J. Klemmer, and T. M. Crawford, J. Appl. Phys. **96**, 2969 (2004).

[52] I. Neudecker, G. Woltersdorf, B. Heinrich, T. Okuno, G. Gubbiotti, and C. Back, J. Magn. Magn. Mater. **307**, 148 (2006).

[53] S. S. Kalarickal, P. Krivosik, M. Wu, C. E. Patton, M. L. Schneider, P. Kabos, T. J. Silva, and J. P. Nibarger, J. Appl. Phys. **99**, 093909 (2006).

[54] H. T. Nembach, T. J. Silva, J. M. Shaw, M. L. Schneider, M. J. Carey, S. Maat, and J. R. Childress, Phys. Rev. B **84**, 054424 (2011).

[55] Here, the value $t_{\mathrm{Co/Au}}$ refers to two independent averaging processes: one is directly connected to the volume averaged nature of the x-ray measurements, which indeed depends on the penetration depth of the beam as well as on its lateral extension; the second one is the arithmetic mean of the thicknesses calculated via the angular position of the first-, second-, and third-order Bragg-like superstructure peaks at low angles.

[56] M Björck and G Andersson, J. Appl. Cryst. **40**, 1174 (2007).

[57] Zs. Czigány and G. Radnóczi, Thin Solid Films **347**, 133 (1999).

[58] M. A. Monclús, M. Karlik, M. Callisti, E. Frutos, J. LLorca, T. Polcar, and J. M. Molina-Aldareguía, Thin Solid Films **571**, 275 (2014).

[59] R. L. Stamps and B. Hillebrands, Phys. Rev. B **43**, 3532 (1991).

[60] A. Kashuba and V. L. Pokrovsky, Phys. Rev. Lett. **70**, 3155 (1993).

[61] A. Berger and H. Hopster, J. Appl. Phys. **79**, 5619 (1996).

[62] C. Kittel, Phys. Rev. **70**, 965 (1946).

[63] M. S. Pierce, J. E. Davies, J. J. Turner, K. Chesnel, E. E. Fullerton, J. Nam, R. Hailstone, S. D. Kevan, J. B. Kortright, Kai Liu, L. B. Sorensen, B. R. York, and O. Hellwig, Phys. Rev. B **87**, 184428 (2013).

[64] D. M. Donnet, K. M. Krishnan, and A. Yajima, J. Phys. D **28**, 1942 (1996).

[65] C. Kooy and U. Enz, Philips Res. Rep. **15**, 7 (1960).

[66] N. Saito, H. Fujiwara, and Y. Sugita, J. Phys. Soc. Jpn. **19**, 1116 (1964).

[67] J. Muller, J. Appl. Phys. **38**, 2413 (1967).

[68] Y. Murayama, J. Phys. Soc. Jpn. **21**, 2253 (1966).

[69] B. Kaplan and G. A. Gehring, J. Magn. Magn. Mater. **128**, 111 (1993).
[70] G. Bertotti, *Hysteresis in Magnetism* (Academic Press, San Diego, 1998).
[71] H. T. Nembach, J. M. Shaw, C. T. Boone, and T. J. Silva, Phys. Rev. Lett. **110**, 117201 (2013).
[72] P. Bruno, J. Magn. Magn. Mater. **121**, 238 (1993).
[73] S. M. Rezende, C. Chesman, M. A. Lucena, A. Azevedo, and F. M. de Aguiar, J. Appl. Phys. **84**, 958 (1998).
[74] T. Kingetsu and K. Sakai, Phys. Rev. B **48**, 4140 (1993).
[75] H. Fritzsche, J. Kohlhepp, and U. Gradmann, J. Magn. Magn. Mat. **148**, 154 (1995).
[76] R. A. Gallardo, P. Alvarado-Segue, T. Schneider, C. Gonzalez-Fuentes, A. Roldán-Molina, K. Lenz, J. Lindner, and P. Landeros, New J. Phys. **21**, 033026 (2019).
[77] Y. Henry, O. Gladii, and M. Bailleul, arXiv:1611.06153.
[78] V. Sluka, T. Schneider, R. A. Gallardo, A. Kákay, M. Weigand, T. Warnatz, R. Mattheis, A. Roldán- Molina, P. Landeros, V. Tiberkevich, A. Slavin, G. Schütz, A. Erbe, A. Deac, J. Lindner, J. Raabe, J. Fassbender, and S. Wintz, Nat. Nanotechnol. **14**, 328 (2019).
[79] Z. K. Wang, V. L. Zhang, H. S. Lim, S. C. Ng, M. H. Kuok, S. Jain, and A. O. Adeyeye, Appl. Phys. Lett. **94**, 083112 (2009).
[80] K. Chesnel, A. S. Westover, C. Richards, B. Newbold, M. Healey, L. Hindman, B. Dodson, K. Cardon, D. Montealegre, J. Metzner, T. Schneider, B. Böhm, F. Samad, L. Fallarino, and O. Hellwig, Phys. Rev. B **98**, 224404 (2018).
[81] T. Emoto, N. Hosoito, and T. Shinjo, J. Magn. Magn. Mater. **189**, L136 (1998).
[82] A. Paul, N. Paul, J. Jutimoosik, R. Yimnirun, S. Rujirawat, B. Höpfner, I. Lauermann, M. Lux-Steiner, S. Mattauch, and P. Böni, Phys. Rev. B **87**, 014431 (2013).
[83] L. Reichel, G. Giannopoulos, S. Kauffmann-Weiss, M. Hoffmann, D. Pohl, A. Edström, S. Oswald, D. Niarchos, J. Rusz, L. Schultz, and S. Fähler, J. Appl. Phys. **116**, 213901 (2014).
[84] J. A. Arregi, J. B. González-Díaz, O. Idigoras, and A. Berger, Phys. Rev. B **92**, 184405 (2015).
[85] C. K. Lo, Y. Liou, C. P. Chang, I. Klik, and Y. D. Yao, and J. C. A. Huang, Appl. Phys. Lett. **68**, 2155 (1996).
[86] W. Yang, D. N. Lambeth, and D. E. Laughlin, J. Appl. Phys. **87**, 6884 (2000).
[87] V. Sokalski, D. E. Laughlin, and J.-G. Zhu, J. Appl. Phys. **110**, 093919 (2011).